Supporting Information for "Flood plain inundation modeling with explicit description of land surface macrostructures"

Simone Pizzileo[1], Giovanni Moretti[1], Stefano Orlandini[1]

[1]Dipartimento di Ingegneria Enzo Ferrari, Università degli Studi di Modena e Reggio Emilia, Via Pietro Vivarelli 10, Modena, Italy

Contents of this file

1. Figures S1–S7

2. Table S1

Introduction

The present supporting information includes figures showing simulated and observed data (Figs. S1–S3), flow resistance parameters (Fig. S4), numerical analysis of flood inundation models (Figs. S5 and S6), and corroboration of a simulated flood inundation with observations for the event occurred on 6 December 2020 in northern Italy (Fig. S7).

The determination of flow hydrograph released by the San Cesario flood control reservoir and forcing the downstream Panaro River is described in Fig. S1. The reconstruction of this flow hydrograph is made possible by experimental work carried out for the Panaro

―――――

Corresponding author: Stefano Orlandini, Dipartimento di Ingegneria Enzo Ferrari, Università degli Studi di Modena e Reggio Emilia, Via Pietro Vivarelli 10, 41125 Modena, Italy. (stefano.orlandini@unimore.it)

April 8, 2024, 4:14pm

River system and observed data on breach formation and repair. Water stage elevation (WSE) upstream and downstream the reservoir dam and bottom outlet openings (g1–g9) are reported. The hydrograph released by the San Cesario flood control reservoir reported in Fig. S1 represents the upstream boundary condition of the riverflow propagation model used in this study.

Fig. S2 illustrates the calibration of the Manning flow resistance coefficients for the Panaro River. The calibration of Manning resistance coefficients n ($\mathrm{m}^{-1/3}\,\mathrm{s}$) is obtained by seeking a good fit between simulated and experimental flow rating curves as shown in the top plot of Fig. S2. Different values of n are used for different flow discharge ranges in three different simulations. The comparison between simulated and experimental flow rating curves obtained by setting $n = 0.038\ \mathrm{m}^{-1/3}\,\mathrm{s}$ for the main channel and $n = 0.082\ \mathrm{m}^{-1/3}\,\mathrm{s}$ for the flood plains is shown in the bottom plot of Fig. S2. The Panaro River floods occurred on January 2014 and December 2020 are used.

Fig. S3 illustrates the validation of Panaro River flood propagation model obtained by comparing simulated and observed water stage elevations at the (a) Navicello station and (b) Bomporto station lying upstream and downstream the breach failure, respectively.

Fig. S4 illustrates the spatial distributions of Manning resistance coefficient n employed when (a) DSM and (b) DTM data are used. Different distributions of the Manning resistance coefficient n are used in combination with DSM and DTM data to differentiate the case where land surface macrostructures are described explicitly and n is only used to represent the effects of microstructures from the case where land surface macrostructures are filtered out and n is used to represent the effects of both micro and macrostructures.

Figs. S5 and S6 illustrate some numerical analysis of flood inundation models with the geomorphologically-informed mesh (GIM) having the higher number of cells (173,268). Fig. S5 shows the (a) mean error ME, (b) mean absolute error MAE, and (c) root mean square error RMSE obtained when five different time steps ($\Delta t = 1, 5, 10, 30, 60$ s) are used. Error functions are computed with respect to the most detailed solution obtained for $\Delta t = 1$ s. Fig. S6 shows the volume conservation error e_v obtained when five different time steps ($\Delta t = 1, 5, 10, 30, 60$ s) are used. Error functions are computed with respect to the most detailed solution obtained for $\Delta t = 1$ s.

Fig. S7 compares simulated and observed times of travel of the flood inundation at the acquisition point A in the South urban area of Nonantola (Fig. S7a) and at the acquisition point B in the North rural area of Nonantola (Fig. S7b). Flood inundation times of travel were computed using flood inundation models based on DSM (Figs. S7c and S7d) and DTM (Figs. S7e and S7f) data. The ridge network was extracted for all simulations in a fully automatic manner by using the LANDMARK algorithm, with $S_c = 10$ m^2 and $P_t = 0.25$ m. The comparison between maps describing flood times of travel using DSM- and DTM-based flood inundation models highlights how the explicit description of topographic macrostructures systematically induces a delay in the flood inundation.

Observed times of arrival and lag times are reported in Tab. S1. Acquisition at point A occurred at 11:45, while acquisition at point B occurred at 16:30. The relative errors in flood time of travel in the DSM-based flood inundation model is -5% and -3% for acquisition points A and B, respectively, whereas the error in flood time of travel in the DTM-based flood inundation model is -29% and -28% for acquisitions A and B, respectively. Negative lag times and relative errors indicate that simulated flood inundations

come in advance with respect to observed flood inundations. The obtained results indicate a 25% improvement in the prediction of flood arrival times when using DSM-based flood inundation models in preference to DTM-based flood inundation models.
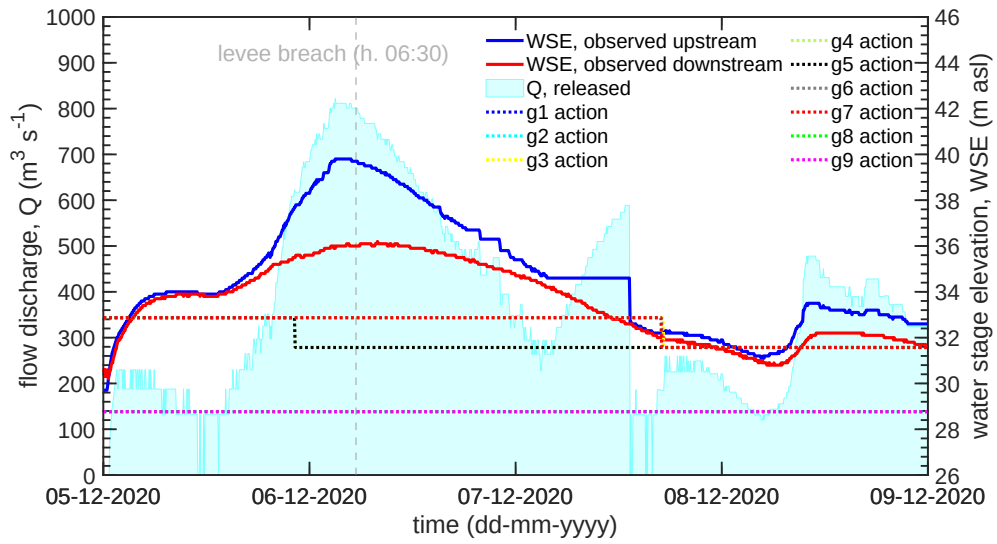
Figure S1. Operation of the San Cesario flood control reservoir during the considered flood inundation event. Water stage elevation (WSE) upstream and downstream the reservoir dam and bottom outlet openings (g1–g9) are reported. The flow hydrograph released by the reservoir (Q) provides the upstream boundary condition for flow propagation along the Panaro River.

April 8, 2024, 4:14pm
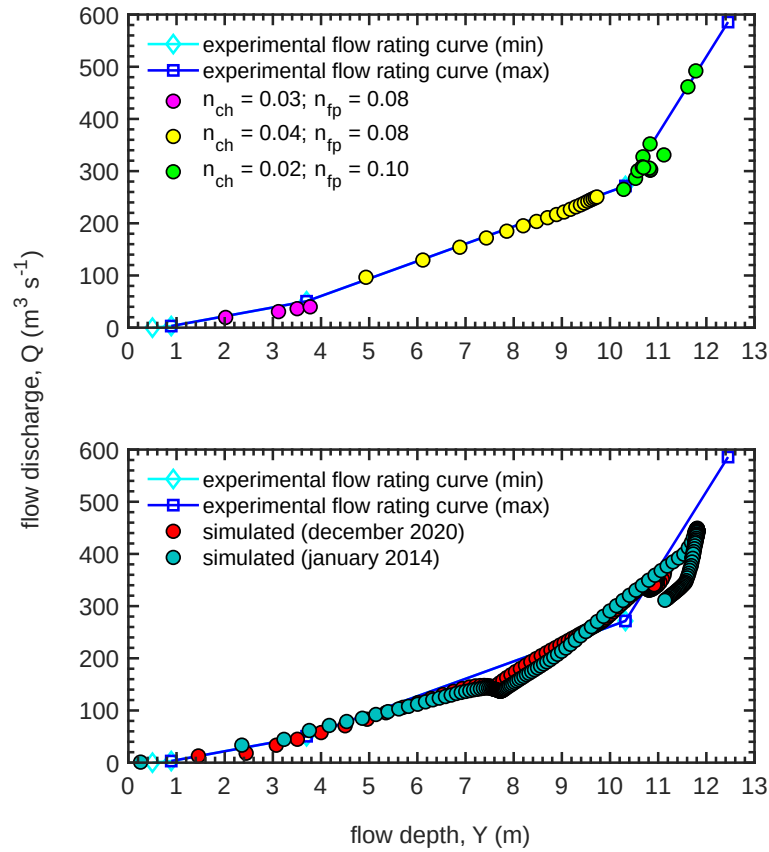
Figure S2. (top plot) Calibration of Manning resistance coefficients n ($\mathrm{m}^{-1/3}$ s) of the Panaro River obtained by seeking a good fit between simulated and experimental flow rating curves. Different values of n are used for different flow discharge ranges in three different simulations. (bottom plot) Comparison between simulated and experimental flow rating curves obtained by setting $n = 0.038$ $\mathrm{m}^{-1/3}$ s for the main channel and $n = 0.082$ $\mathrm{m}^{-1/3}$ s for the flood plains. The Panaro River floods occurred on January 2014 and December 2020 are used.
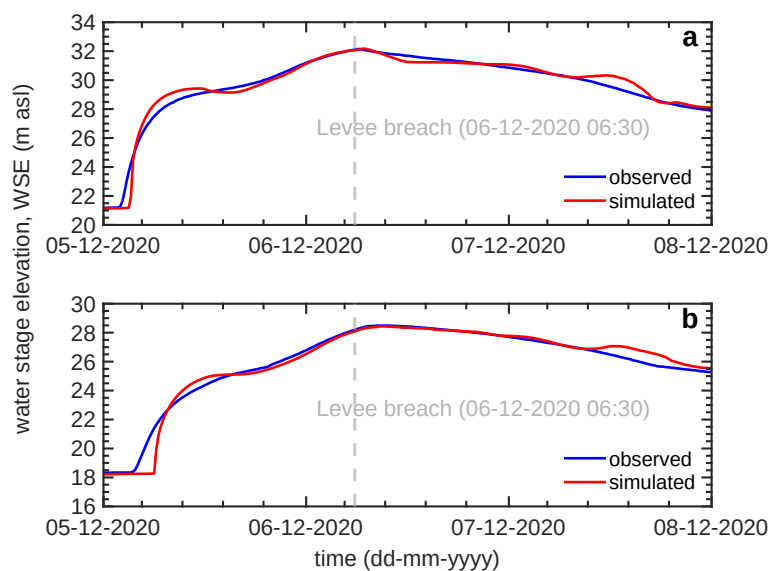
Figure S3. Comparison between observed and simulated water stage elevations in the Panaro River at the (a) Navicello station and (b) Bomporto station lying upstream and downstream the breach failure, respectively.
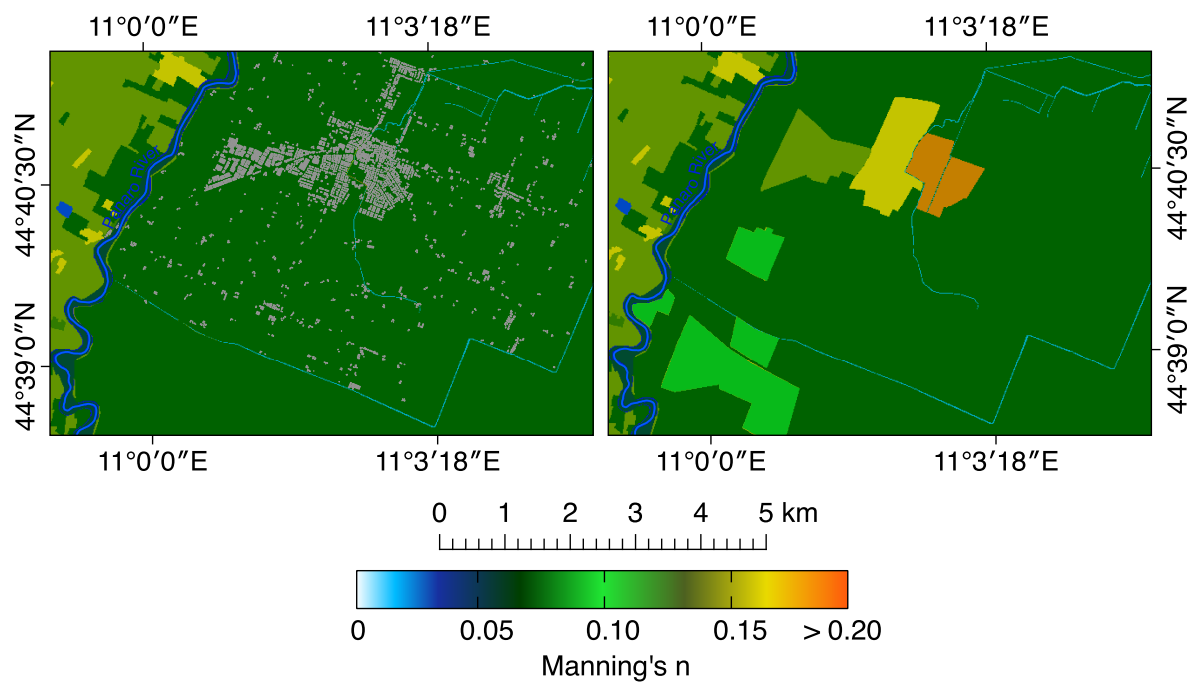

Figure S4. Spatial distributions of Manning resistance coefficient n employed when (a) DSM and (b) DTM data are used.

April 8, 2024, 4:14pm

:
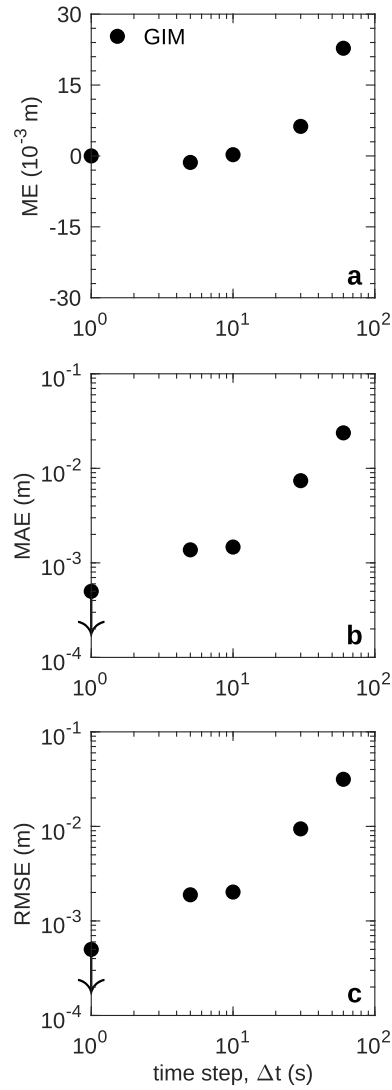
Figure S5. Evaluation of flood inundation models with the geomorphologically-informed mesh (GIM) having the higher number of cells (173,268) in terms of (a) mean error ME, (b) mean absolute error MAE, and (c) root mean square error RMSE, for different time steps ($\Delta t = 1, 5, 10, 30, 60$ s). ME, MAE, and RMSE are computed with respect to the most detailed solution obtained for $\Delta t = 1$ s.
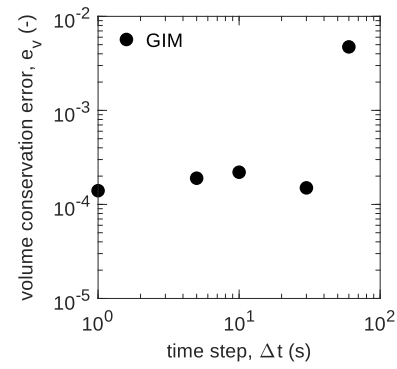
Figure S6. Evaluation of flood inundation models with the geomorphologically-informed mesh (GIM) having the higher number of cells (173,268) in terms of volume conservation error e_v, for different time steps ($\Delta t = 1, 5, 10, 30, 60$ s). e_V is computed with respect to the most detailed solution obtained for $\Delta t = 1$ s.
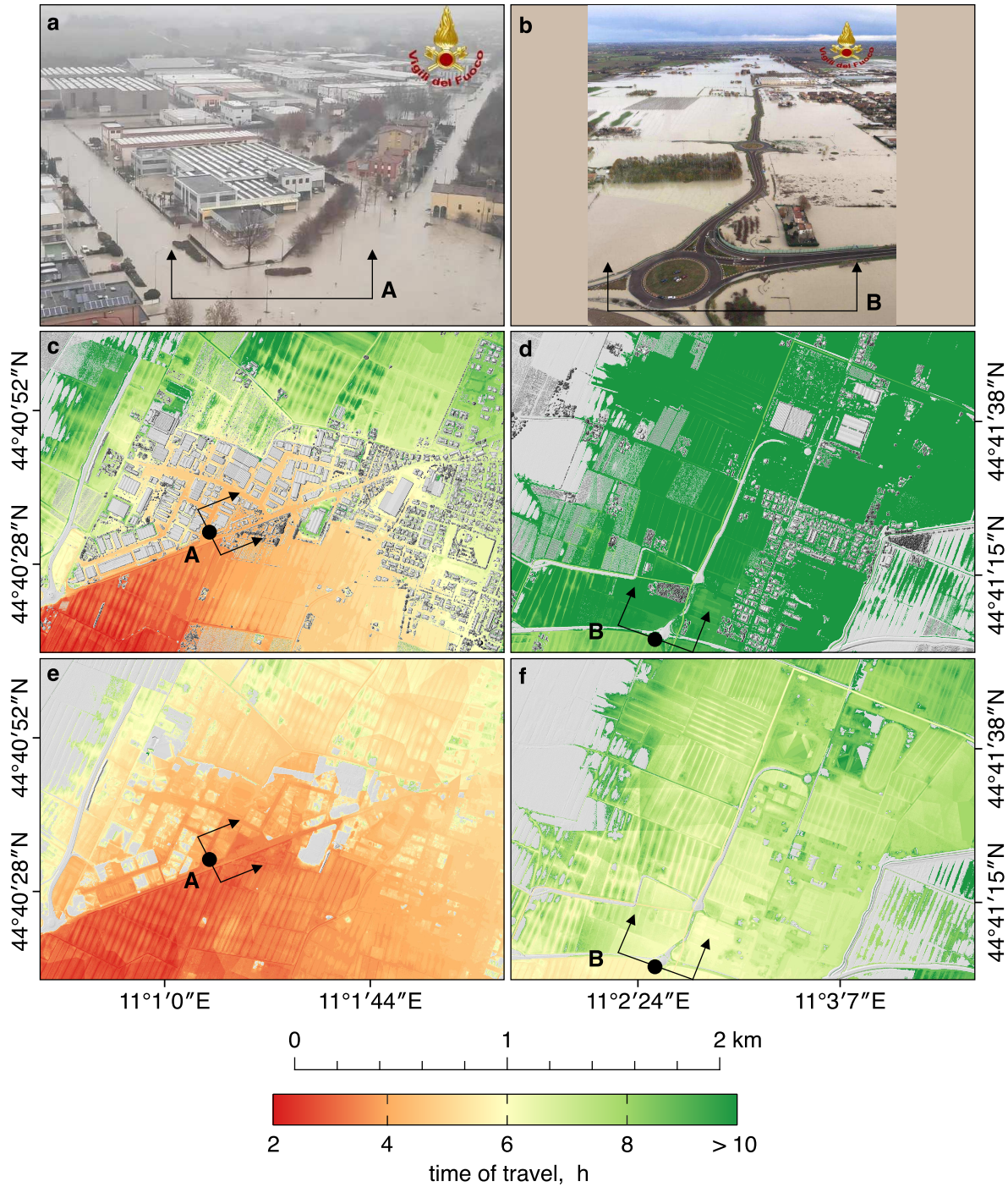
Figure S7. Time of travel of the flood inundation across (a) the South urban area of Nonantola and (b) the North rural area of Nonantola obtained from flood inundation models based on (c and d) digital surface model (DSM) and (e and f) digital terrain model (DTM) data. The capture of photograph A took place on 6 December 2020 at 11:45, whereas the capture of photograph B took place on 6 December 2020 at 16:30 (Tab. S1), corresponding to a lag time after the levee failure of 5.25 and 10.00 h, respectively.

Table S1. Times of arrival, times of travel, lag times, and relative errors in times of travel for flood inundation models based on DSM and DTM data.

	Acquisition Point	
Data source	A	B
Levee Failure (HH:MM)		
Observed	6:30	6:30
Times of Arrival (HH:MM)		
Observed	11:45	16:30
DSM-based model	11:30	16:15
DTM-based model	10:15	13:45
Times of Travel (h)		
Observed	5.25	10.00
DSM-based model	5.00	9.75
DTM-based model	3.75	7.25
Lag Times (h)		
DSM-based model	-0.25	-0.25
DTM-based model	-1.50	-2.75
Relative Errors (%)		
DSM-based model	-5	-3
DTM-based model	-29	-28